Final Report

CHEMISTRY-STRUCTURE-PROPERTY INTERRELATIONSHIPS FOR CALCAREOUS DEPOSITS AS STAND-ALONE COATINGS

(Contract Number N00014-86-K-0144)

submitted to

Office of Naval Research
800 North Quincy Street
Arlington, Virginia 22217

submitted by

Center for Marine Materials
Department of Ocean Engineering
Florida Atlantic University
Boca Raton, Florida 33431

Project Duration: January 15, 1986 - April 30, 1989

Co-Principal Investigators: Dr. William H. Hartt
Dr. Samuel W. Smith

December 7, 1989

SUBSTRATE, SURFACE FINISH AND FLOW RATE INFLUENCES UPON CALCAREOUS DEPOSIT STRUCTURE AND PROPERTIES

Katherine E. Mantel*
Naval Surface Warfare Center
Ft. Lauderdale, Florida 33315

William H. Hartt
Center for Marine Materials
Florida Atlantic University
Boca Raton, Florida 33431

and

Tzu-Yu Chen**
Nalco Chemical Company
Naperville, Illinois 60563

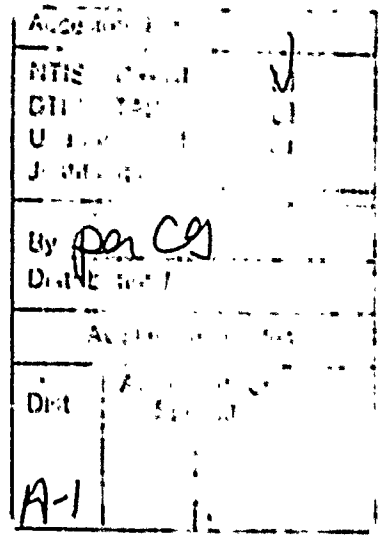

ABSTRACT

Experiments have been performed where 1018, A710, A537 and HY80 steel specimens of surface finish corresponding to #120, 320, 600 and 1500 polishing were polarized potentiostatically in seawater at -900 mv (SCE). The resulting calcareous deposits were analyzed with regard to structure, composition and morphology and found to be comprised of a relatively thin inner Mg rich layer which formed initially and a subsequent, thicker, outer aragonite precipitate. The effect of this dual deposit structure, as well as variations in substrate, surface finish and electrolyte flow rate, upon current density decay was evaluated; and the observed trends are discussed in terms of the film formation process and cathodic protection utility.

INTRODUCTION

Calcareous deposits are a relatively unique type of surface film comprised primarily of $CaCO_3$ and $Mg(OH)_2$ which precipitate upon cathodic surfaces in seawater. This occurs as a consequence of increased pH near the metal-electrolyte interface in association with the reactions

---

* Formerly Graduate Student, Florida Atlantic University
** Formerly Postdoctoral Associate, Florida Atlantic University

$$1/2\ O_2 + H_2O + 2e^- \rightarrow 2OH \text{ and/or} \quad (1$$

$$2H_2O + 2e^- \rightarrow 2H + 2OH^- \quad (2$$

which, in turn, alter the inorganic carbon equilibria

$$CO_2 + H_2O \rightarrow H_2CO_3, \quad (3$$

$$H_2CO_3 \rightarrow H^+ + HCO_3^- \text{ and} \quad (4$$

$$HCO_3^- \rightarrow H^+ + CO_3^{2-} \quad (5$$

thereby facilitating the reaction

$$OH^- + HCO_3 \rightarrow H_2O + CO_3^{2-}. \quad (6$$

As a consequence of 1) or 2) (or both) the equilibrium

$$Mg^{+2} + 2(OH^-) \rightarrow Mg(OH)_2 \quad (7$$

is displaced to the right, and because of 6) precipitation of $CaCO_3$ is enhanced.

The importance of calcareous deposits to the effective, efficient operation of marine cathodic protection systems is generally recognized by engineers and scientists concerned with cathodic protection in submerged marine environments. Despite the contribution provided by recent research activities in this area (1-4) a basic understanding of deposits is still lacking. Also of interest is how the protective capacity of calcareous deposits can be optimized. The present paper reports the results of research that was intended to investigate the influence of ferrous alloy substrate and surface finish variations upon the calcareous deposit formation process and properties. In the process of doing this research certain features of these surface films were disclosed which potentially have a broader impact upon understanding the composition/structure - property interrelationships of these precipitates.

EXPERIMENTAL PROCEDURE

Specimens: The test material for the experiments was 1018, HY80, A710 and A537 steels, the composition for each being as listed in Table I. Specimens of a 13 mm OD/6 mm ID by 25 mm long cylindrical geometry were machined from these followed by progressive polishing with SiC paper wetted with mineral oil to the desired surface finish. This was followed by an acetone rinse, air drying and mounting on a stainless steel rod between two Delrin washers, as shown by Figure 1. Immediately preceding the experiment each specimen was repolished with the final finish polishing paper, ultrasonically cleaned, acetone rinsed and air dried.

Electrochemical Cell: A series of four electrochemical cells were employed, each of which involved a standard 600 ml glass beaker and a Plexiglas cap with ports for the 1) working electrode, 2) a Pt coated Nb mesh counter electrode, 3) saturated calomel reference electrode, 4) thermometer and 5) seawater inlet and exhaust. The cells were immersed in a constant temperature bath such that temperature for all experiments was in the range 24 ± 2°C. This bath was not employed for a limited number of short term experiments for which temperature in any given case was constant within 1°C and in the range 24-28°C. Figure 2 schematically illustrates the arrangement for an individual cell. The electrolyte

was sand filtered, natural sea water, the properties of which have been reported previously for an annual cycle (5). Cathodic polarization was maintained at -900±2 mv, SCE, throughout the experiments utilizing locally fabricated potentiostats based upon the circuitry of Baboian et al (6).

General Procedure: Initial cell set-up involved establishment of the desired flow rate and polarization of a dummy specimen of the same material as the working electrode in question to -900 mv. Subsequently, the actual working electrode was concurrently immersed and polarized. Potential and current data were recorded at intervals ranging from 10 seconds to two hours by an Esterline Angus Model PD 2064 data acquisition system. Upon termination of an experiment the specimen was rinsed with distilled water and acetone, air dried, disassembled from the mounting rod and stored in a vacuum desiccator. Compositional and morphological studies utilized an EG&G ORTEC System 5000 and ISI Super IIIA SEM. Film crystallography was identified using a Phillips Model 3600 X-ray diffraction unit.

RESULTS AND DISCUSSION

Substrate and Surface Finish Effects: Figures 3-6 present current density versus time plots to 8400 minutes for the different surface finishes of each of the four steels. In a generalized sense the 1018 and A710 data were characterized by a sigmoidal curve involving 1) an upper plateau of approximately constant current density to about 2000 minutes, 2) a transition regime of current density decay (2000-4000 minutes) and 3) a lower plateau of constant current density in the range 25-100 mA/m^2 (time > 4000 minutes). This trend is in general accord with that reported previously by others (1,3,7-9). Note also that the current density for the lower plateau is in general agreement with the design current density for quiescent water marine cathodic protection (10). The upper plateau was less distinct for A537 (Figure 5) and HY80 (Figure 6). At the same time the 1018/#120 data (Figure 3) exhibited current density-time behavior analogous to that for HY80 of all four surface finishes. The observation from Figures 4 and 5 that there was nothing distinctive for the #120 surface finish for A710 and A537 steel specimens suggests that surface roughness per se was probably not responsible for the unique 1018/#120 behavior and that the relatively low upper plateau current density for this test condition was due to some other factor.

It is generally recognized that the current density to polarize steel to relatively modest cathodic potentials in seawater is determined by dissolved oxygen availability as affected, first, by oxygen concentration polarization and, second, by calcareous deposits. Development of oxygen concentration polarization probably influenced the upper plateau current density; and deposits were important subsequently in the process, as will be demonstrated later. While the present experiments involved an electrolyte replenishment rate of 100 ml/min for 1018, A710 and A537 steels, the value for HY80 was 40 ml/min. Previous research has shown that current density required to cathodically polarize steel in seawater varies in direct proportion to velocity during the initial period of exposure, consistent with the anticipated role of oxygen concentration polarization (11). Flow rate difference may have been responsible for the lower initial current density of HY80 (170-330 mA/m^2) compared to the other steels where this parameter was in the range 270-540 mA/m^2. With this possibility in mind it was concluded that there were no trends in the present data to indicate a dependence of current density decay upon either substrate or surface finish. At more negative potentials, where the hydrogen reaction becomes progressively of greater importance, low overvoltage

cathodic sites which differ according to substrate could establish a varied local electrolyte composition and in so doing modify deposit formation kinetics.

Deposit Morphology and Composition: The morphology of all specimens was studied after the 8400 minute exposure. While the general appearance of these was similar to what has been reported by others (1,3,8,9) for steel exposed under comparable conditions, distinctive morphological size scale variations were apparent, as illustrated by the examples in Figure 7a-c. Interestingly, there was a direct correspondence between deposit size and upper plateau current density. Thus, the morphology in Figure 7a, was observed for 1018/#320, 600 and 1500, A710/#120, 320, 600, and 1500 and A537/#600. In each of these cases the upper plateau current density was near or greater than 400 mA/m^2. The deposit appearance in Figure 7b, on the other hand, was observed for A537/#120, 320 and 1500, for which the upper plateau current density was in the approximate range 325-400 mA/m^2. All HY80 surface finishes as well as 1018/#120 corresponded in appearance to Figure 7c for which current density in the pre-2000 minute period was typically below 3[illegible] mA/m^2.

Compositional analyses revealed the predominant cation to be Ca^{+2} with minor amounts (< 6 w/o each) of Mg, Sr, Fe, Cl, S, Si and Na also being detected. No consistent compositional trend for any of these components was apparent with regard to substrate or surface finish. X-ray diffraction analysis of powder samples collected from specimens exemplifying the three morphology types (Figure 7) revealed these to be predominantly aragonite in each case.

Deposit Evolution: Not apparent from Figures 3-6 because the compressed time scale is an initial, relatively abrupt current density decay which was noted for all substrate/surface finish combinations during the initial minute of exposure. This is illustrated by Figure 8 for the specific case of A710/#600. To investigate the evolutionary nature of deposits, both during and subsequent to this initial decay, a separate experiment was performed upon a series of 1018/#600 specimens, each of which was polarized to -900 mV with individual tests being terminated at 0.4, 2, 60, 1000, 2000, 3000, 4000, 6000, and 8400 minutes (nominal). Figure 9 reports the current density for the longer term specimens just prior to removal from the solution and reveals a general current density decay trend similar to that in Figures 3 and 4. The 0.4 and 2 minute termination times were selected as representative of the initial current density decay period (Figure 8). Correspondingly, the 60, 1000 and 2000 minute specimens were intended to exemplify the beginning, mid-point and terminus of the upper plateau, whereas the 4000, 6000 and 8400 minute ones were for these same hallmarks on the lower plateau. The 3000 minute specimen, on the other hand, fell at about the mid-point of the second current density decay.

Figures 10-12 present micrographs of the specimens exposed for 0.4, 2 and 60 minutes, respectively. EDAX analysis revealed each of these surfaces to be uniformly covered by a Mg-rich film (presumably $Mg(OH)_2$). The individual particles which are also apparent in these figures were predominantly Mg. Figure 13 presents a micrograph of a short term exposure specimen where the Mg-rich film debonded, thereby revealing the thin, uniform nature of this precipitate. The relative role of oxygen concentration polarization, as opposed to film formation in causing the initial current density drop (1400 to 500 mA/m^2, Figure 8) was investigated by performing several parallel experiments in both seawater and a 3.5 w/o NaCl - distilled water solution. Figure 14 exemplifies the results of these and reveals significant current density drop in the NaCl solution where film formation should not occur. The upper plateau current density was approximately 275 mA/m^2 less in

seawater than NaCl - distilled water, however; and this difference must be ascribed to the Mg-rich film in the former case. Thickness of this film was calculated as approximately 10^{-8}m by assuming all hydroxides produced via Equations 1 and 2 prior to current density achieving the upper plateau value formed $Mg(OH)_2$. However, this calculation has not considered 1) possible film porosity, 2) the pH increase from ambient to about 9.5 and 3) reaction of OH^- by Equation 6. Consequently, this result must be considered as an order-of-magnitude estimate only.

Figures 15-20 present micrographs of the morphologies for 1000 to 8400 minutes and record the progressive occurrence of $CaCO_3$ precipitation (relatively large particles). The shorter time deposit structures (1000 and 2000 minutes) were comprised primarily of individual, isolated particles, whereas at greater times (4000 minutes and beyond) these have grown together and covered almost the entire surface. For the intermediate times (2000-4000 minutes) deposit development involved progressive particle impingement. Correspondence of this period with the second current density decay (Figures 3-6) indicates that it was this growing together of particles which provided the oxygen diffusion barrier that resulted in the final, lower plateau current density. The fact that current density was relatively constant prior to 2000 minutes suggests that the separate, unit $CaCO_3$ particles had little or no effect upon net oxygen availability and that impingement was required for current density reduction.

The observation that the lower plateau current density did not depend upon substrate or surface finish and was approximately the same for both 100 ml/min (Figures 3-5) and 40 ml/min (Figure 6) replenishment rates indicates that the effective resistance of the deposits to oxygen diffusion was independent of these factors (substrate, surface finish and flow rate). This conclusion in the case of flow rate is consistent with the results of others who have shown cathodic current density, once deposit formation has taken place, to be velocity independent provided the coating has not been mechanically disturbed (11,12). The deposit morphological differences (Figure 7), which were projected to result from distinctions in the initial or upper plateau current densities, had no apparent influence upon oxygen diffusivity. Analysis of the long term (8400 minutes) film revealed only minor amounts of Mg, as discussed earlier. However, stripping of deposits from the substrate and analysis of the underside revealed that an inner Mg-rich layer was present (13). This was confirmed by frontal, spot analysis of local areas where the outer layer, Ca-rich particles had not impinged. Thus, the final calcareous deposit which formed upon the present specimens involved a relatively thin, uniform Mg-rich inner layer which was probably $Mg(OH)_2$ and a thicker, outer layer of interlaced aragonite particles.

It is generally recognized that $Mg(OH)_2$ is undersaturated in seawater for ambient conditions and tends to precipitate only for pH > 9.5. Calcium carbonate, either as aragonite or calcite, has a lower solubility product than for $Mg(OH)_2$ and is supersaturated under near-surface conditions. Precipitation kinetics for $CaCO_3$ are, however, slower than for $Mg(OH)_2$ due to an inhibiting influence of Mg^{++} upon aragonite nucleation and upon both nucleation and growth of calcite (14). These factors explain the observation that 1) the initial film which precipitated was Mg-rich and 2) $CaCO_3$ formed predominantly as aragonite rather than the more stable calcite.

It has been previously projected that magnesium depletion in association with $Mg(OH)_2$ precipitation is a precursor to $CaCO_3$ formation (2,3). However, Sadasiran (15) has reasoned that this does not occur once steady-state has been established due to relatively high $[Mg^{++}]$ in seawater compared to $[OH^-]$, such that

precipitation of $Mg(OH)_2$ is under OH^- and not Mg^{++} concentration control. Thus, pH near the metal-electrolyte interface should rise only slightly above 9.5 (assumed pH corresponding to the $Mg(OH)_2$ solubility limit) and $[Mg^{++}]$ should not be significantly different from the saturation value at that pH. Although precipitation of the Mg-rich film occurred readily during the initial few seconds of exposure, its development was limited in association with the modest electrolyte layer thickness within which pH was such that $[Mg^{++}][OH^-]^2 > K_{sp}$. The reporting by others of more rapid $CaCO_3$ precipitation in Mg^{++} free synthetic seawater compared to solutions where this cation was present (2,3) is probably related to the enhanced buffering capacity of the latter solution (seawater) and correspondingly reduced pH and driving force for precipitation. Instead of $CaCO_3$ formation kinetics being influenced by Mg^{++} depletion, it is more likely that sufficient Mg^{++} existed in the near-interface electrolyte to eliminate calcite nucleation and limit aragonite nucleation to the extent observed microscopically (see Figures 10-16). However, once a particle of this phase achieved critical size, growth was rapid due to the relatively high supersaturation level which exists at pH ~ 9.5. The microscopic evidence (Figure 7) supports this low nucleation-high growth rate projection. Also, the reporting of increased particle size at higher current density (alternately, flow rate) is consistent with lower nucleation rate for this condition, since pH gradient should be more steep and OH^- less concentrated in the diffusion boundary layer at higher velocity.

Effect of Velocity upon Initial Precipitation. The observation from comparison of the current density-time trend for 40 ml/min (Figure 6) and 100 ml/min specimens (Figures 3-5) suggests that flow rate was influential with regard to the upper plateau current density. On this basis it is possible that an undisclosed low velocity condition existed for testing of the 1018/#120 specimen (Figure 3) and that the exceptional current density trend for this experiment was a consequence of this. Flow rate variations of a lesser degree could have accounted for the more modest specimen-to-specimen differences apparent in Figures 3-6. On this basis a series of short term tests were performed upon HY80/#600 specimens with flow rate in the range 20-380 ml/min. Figure 21 reports the results of these and shows that, while initial current density was the same in each case according to the bulk oxygen concentration the upper plateau current density varied in general in direct proportion to flow rate. Figure 22 plots upper plateau current density versus flow rate for all experiments, including those in Figures 3-6, 8 and 21 and shows a direct, linear dependence of the former upon the latter. Such an observation must be related either to differences in dissolved oxygen transport through the $Mg(OH)_2$ film or in the diffusional boundary layer beyond the film or both. To investigate this a series of experiments was performed where flow rate was increased subsequent to formation of the Mg-rich film and the accompanying current density change recorded. Figure 23 reports the results where one specimen each of HY80/#600 was exposed to a flow rate of 22, 260 or 300 ml/min for the initial 10 minutes, followed by 10 minutes at 400 ml/min and finally returned to to the original value. Consistent with Figure 22 the current density varied in proportion to flow rate and was the same in each case during the 400 ml/min period. This indicates either that the resistance of the Mg-rich film to oxygen diffusion was the same in each case or that the film thickness varied inversely and changed reversibly with flow rate as a result of precipitation/dissolution. That current density on the lower plateau was velocity independent (Figures 3-6 and reference 11) was probably due to the film here being sufficiently thick and resistive compared to the electrolyte diffusional boundary layer that significance of the latter was negligible.

This research indicates that although the inner Mg-rich layer was a small

contributor to the overall deposit thickness, it was still important since it is upon this that $CaCO_3$ precipitates formed. On this basis subsequent research should focus upon if and how modifications to the inner layer affect the structure and properties of aragonite precipitation.

CONCLUSIONS

Within the range of experimental parameters investigated the following conclusions have been made:

1. A uniform Mg-rich film formed within the initial minute or so of polarization. Despite being relatively thin ($\sim 10^{-8}$m) this film significantly reduced oxygen flux to the cathode. The steady-state cathodic current density associated with the film increased in proportion to flow rate.

2. Nucleation and growth of $CaCO_3$ occurred at a slower rate than for the Mg-rich film, such that the final calcareous deposit was a composite of a relatively thin, inner Mg-rich layer and a thicker, outer one of aragonite. Morphology of $CaCO_3$ was more course the higher the current density, actually flow rate, apparently due to a more steep $[OH^-]$ gradient and reduced driving force for nucleation. $CaCO_3$ influenced oxygen flux and current density only after the individual particles impinged upon one another, which required an exposure time > 2000 min. Once this growing together was nearly completed, current density stabilized at a second, lower value which was comparable to marine cp design current densities and independent of flow rate.

3. Calcareous deposit structure and properties and current density decay were essentially the same for 1018, A710, A537 and HY80 substrates and for surface finishes corresponding to #120, 320, 600 and 1500 polishing. This was attributed to the fact that, first, the pH increase near the metal surface occurred in association with oxygen reduction and, second, aragonite formed upon the Mg-rich film and not the steel per se.

ACKNOWLEDGEMENTS

The authors are indebted to Drs. S. W. Smith and R. U. Lee for critical discussions of this research and to the Office of Naval Research Contract No. N00014-86-K-0144 for financial support.

BIBLIOGRAPHY

1. S. L. Wolfson and W. H. Hartt, Corrosion, Vol. 37, 1981, p. 70.

2. S-H. Lin and S. C. Dexter, Corrosion, Vol. 44, 1988, p. 615.

3. J. S. Luo, R. U. Lee, T. Y. Chen, W. H. Hartt and S. W. Smith, "Formation of Calcareous Deposits under Different Modes of Cathodic Protection," paper no. 36 presented at CORROSION/88, March 21-25, 1988, St. Louis, to be published in Corrosion.

4. J. E. Finnegan and K. P. Fischer, "Calcareous Deposits: Calcium and Magnesium Ion Concentrations," paper no. 581 presented at CORROSION/89, April 17-21, 1989, New Orleans.

5. W. H. Hartt, "Fatigue of Welded Structural Steel in Seawater," Proc. Thirteenth Annual Offshore Tech. Conf., 1981, Houston, p. 87.

6. R. Baboian, L. McBride, R. Langlais and G. Haynes, Materials Performance, Vol. 18(12), 1979, p. 40.

7. T. L. Nye, S. W. Smith and W. H. Hartt, ASTM Spec. Tech. Pub. 866, 1985, p. 207.

8. M. M. Kunjapur, W. H. Hartt and S. W. Smith, Corrosion, Vol. 43, 1987, p. 674.

9. W. Mao and W. H. Hartt, "Growth Rate of Calcareous Deposits in Seawater," paper no. 317 presented at CORROSION/85, March 15-19, 1985, Boston.

10. "Recommended Practice -Control of Corrosion on Steel, Fixed Offshore Platforms Associated with Petroleum Production," NACE Standard RP-01-76, Natl. Assn. Cor. Engrs., April, 1976.

11. P. O. Gartland, R. Strommen and E. Bardol, Materials Performance, Vol. 22(6), 1983, p. 40.

12. W. H. Hartt and N. K. Lin, "An Evaluation of Calcareous Deposits As Affected by Seawater Movements," Proc. Offshore Mech. and Arctic Engr. Conf., 1987, Houston, p. 196.

13. J. S. Luo, Florida Atlantic University, Boca Raton, Florida, unpublished research.

14. G. K. Sadasivan, "Computer Simulation of Calcareous Deposits," M. S. Thesis, Florida Atlantic University, Boca Raton, Florida, 1989.

15. C. H. Culberson, "Effect of Seawater Chemistry on the Formation of Calcareous Deposits," paper no. 61 presented at CORROSION/83, April 18-22, 1983, Anaheim.

Figure Captions

Figure 1. Schematic illustration of specimen holder.

Figure 2. Electrochemical cell arrangement.

Figure 3. Current density versus time curves for 1018 steel specimens of four different surface finishes concurrently polarized in seawater at -900 mV and 100 ml/min flow rate.

Figure 4. Current denisity versus time curves for A710 steel specimens of four different surface finishes concurrently polarized in seawater at -900 mV and 100 ml/min flow rate.

Figure 5. Current density versus time curves for A537 steel specimens of four different surface finishes concurrently polarized in seawater at -900 mV and 100 ml/min flow rate.

Figure 6. Current density versus time curves for HY80 steel specimens of four different surface finishes concurrently polarized in seawter at -900 mV and 40 ml/min flow rate.

Figure 7. Scanning electron micrograph of calcareous deposits on specimens polarized to -900 mV at seawater refreshment rate of 100 ml/min for 8400 min. (a) A710/#120 steel, (b) A537/#320 steel and (c) 1018/#120 steel.

Figure 8. Typical current density versus time curve for the first 10 minutes of polarization to -900 mV. A710/#600, seawater refreshment rate of 100 ml/min.

Figure 9. Current density versus time curve for 1018/#600 steel polarized to -900 mV for 8400 minues. Data points are the final i values for specimens exposed for 1000, 2000, 3000, 4000 and 6000 minutes.

Figure 10. Scanning electron micrograph of calcareous deposits on 1018/#600 steel polarized to -900 mV for 0.4 minutes at seawater refreshment rate of 100 ml/min.

Figure 11. Scanning electron micrograph of calcareous deposits on 1018/#600 steel polarized to -900 mV for two minutes at seawater refreshment rate of 100 ml/min.

Figure 12. Scanning electron micrograph of calcareous deposits on 1018/#600 steel polarized to -900 mV for 60 minutes at seawater refreshment rate of 100 ml/min.

Figure 13. Scanning electron micrograph of partially disbonded calcareous film on 1018/#600 steel polarized to -900 mV for 15 minutes at seawater refreshment rate of 100 ml/min.

Figure 14. Current density versus time curves for polarization of HY80/#600 steel in 3.5 w/o NaCl and in natural seawater at -900 mV and refreshment rate of 100 ml/min.

Figure 15. Scanning electron micrograph of Calcareous deposits on 1018/#600 polalrized to -900 mV for 1000 minutes at seawater refreshment rate of 100 ml/min. (a) low magnification and (b) high magnification.

Figure 16. Scanning electron micrograph of calcareous deposits on 1018/#600 polarized to -900 mV for 2000 minutes at seawater refreshment rate of 100 ml/min. (a) low magnification and (b) high magnification.

Figure 17. Scanning electron micrograph of calcareous deposits on 1018/#600 polarized to -900 mV for 3000 minutes at seawater refreshment rate of 100 ml/min. (a) low magnification and (b) high magnification.

Figure 18. Scanning electron micrograph of calcareous deposits on 1018/#600 polarized to -900 mV for 4000 minutes at seawater refreshment rate of 100 ml/min. (a) low magnification and (b) high magnification.

Figure 19. Scanning electron micrograph of calcareous deposits on 1018/#600 polarized to -900 mV for 6000 minutes at seawater regfreshment rate of 1000 ml/min. (a) low magnification and (b) high magnification.

Figure 20. Scanning electron micrograph of calcareous deposits on 1018/#600 polarized to -900 mV for 8400 minutes at seawater refreshment rate of 100 ml/min. (a) low magnification and (b) high magnification.

Figure 21. Current density versus time curves for HY80/#600 specimens polarized to -900 mV at seawater refreshment rates of 20, 40, 100, 200 and 380 ml/min.

Figure 22. Plot of upper current density plateau values vs. seawater refreshment rate for all experiments.

Figure 23. Current density versus time curves for HY80/#600 specimens polarized to -900 mV. Each specimen was exposed to flow rates of 22, 260, or 300 ml/min for the initial 10 min. followed by 10 min. at 400 ml/min and then returned to the initial flow rate.

TABLE I

Composition of Test Materials

Weight %

	C	Si	Mn	P	S	Cu	Ni	Cr	Mo	Nb	V	Ti	N	Al(sol)
1018	0.166	0.194	0.738	0.009	0.019	0.197	0.105	0.096	0.064	-	-	-	-	-
A710	0.040	0.300	0.450	0.004	0.002	1.140	0.820	0.670	0.180	0.037	0.004	0.002	0.0047	0.034
A537	0.120	0.410	1.300	0.014	0.003	0.010	0.030	0.040	0.05	-	0.044	-	-	-
HY80	0.130	0.160	0.280	0.005	0.005	0.020	3.080	1.700	0.44	-	0.006	0.004	0.009	0.019

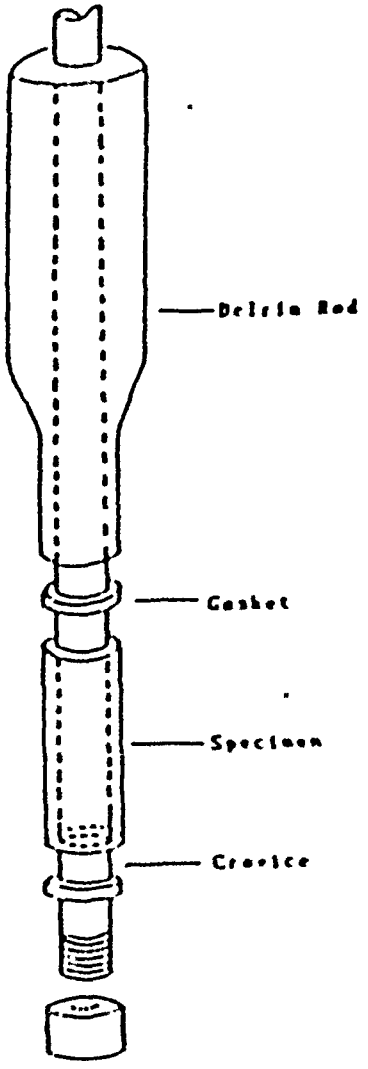

Figure 1. Schematic illustration of specimen holder.

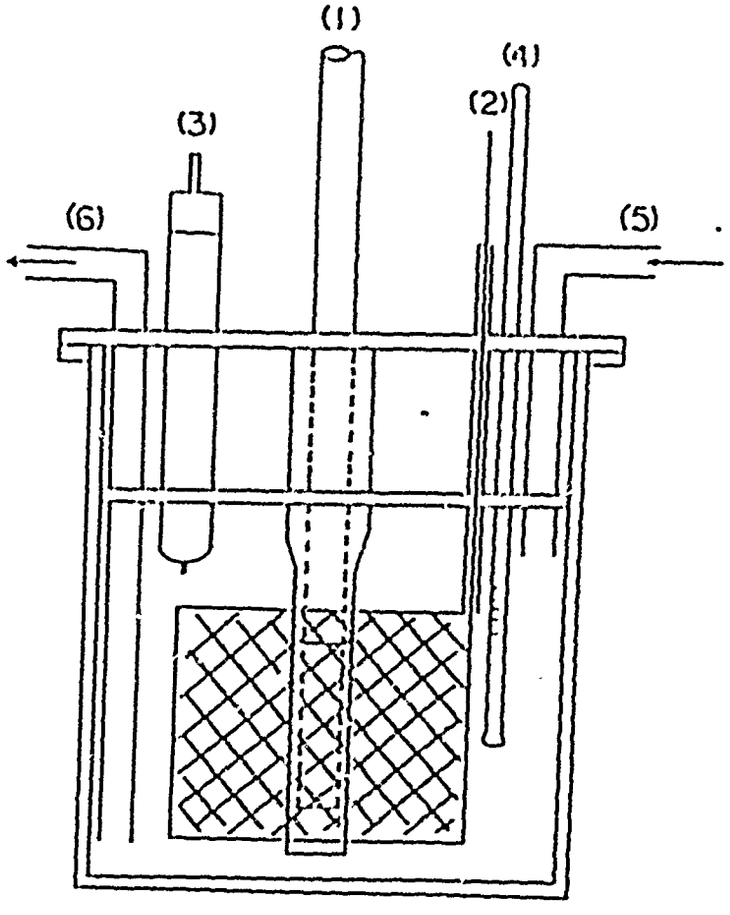

1). Specimen Holder
2). Counter Electrode
3). Reference Electrode
4). Thermometer
5). Solution Inlet
6). Solution Outlet

Figure 2. Electrochemical cell arrangement.

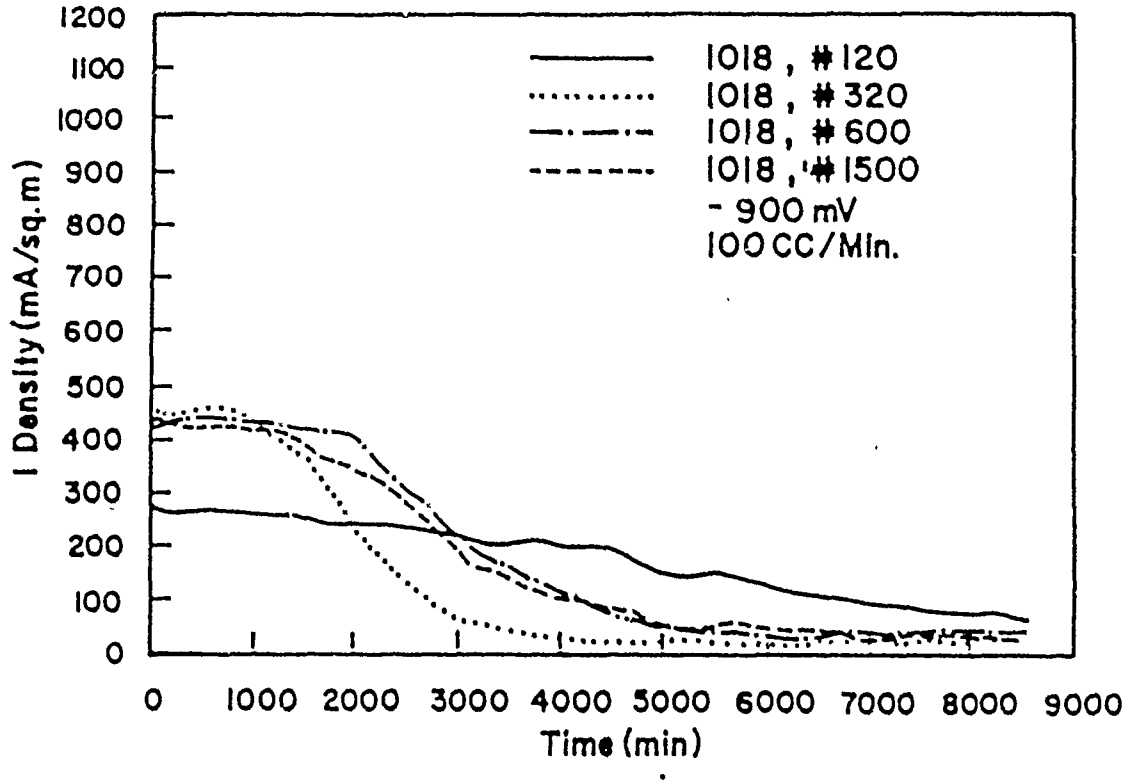

Figure 3. Current density versus time curves for 1018 steel specimens of four different surface finishes concurrently polarized in seawater at -900 mV and 100 ml/min flow rate.

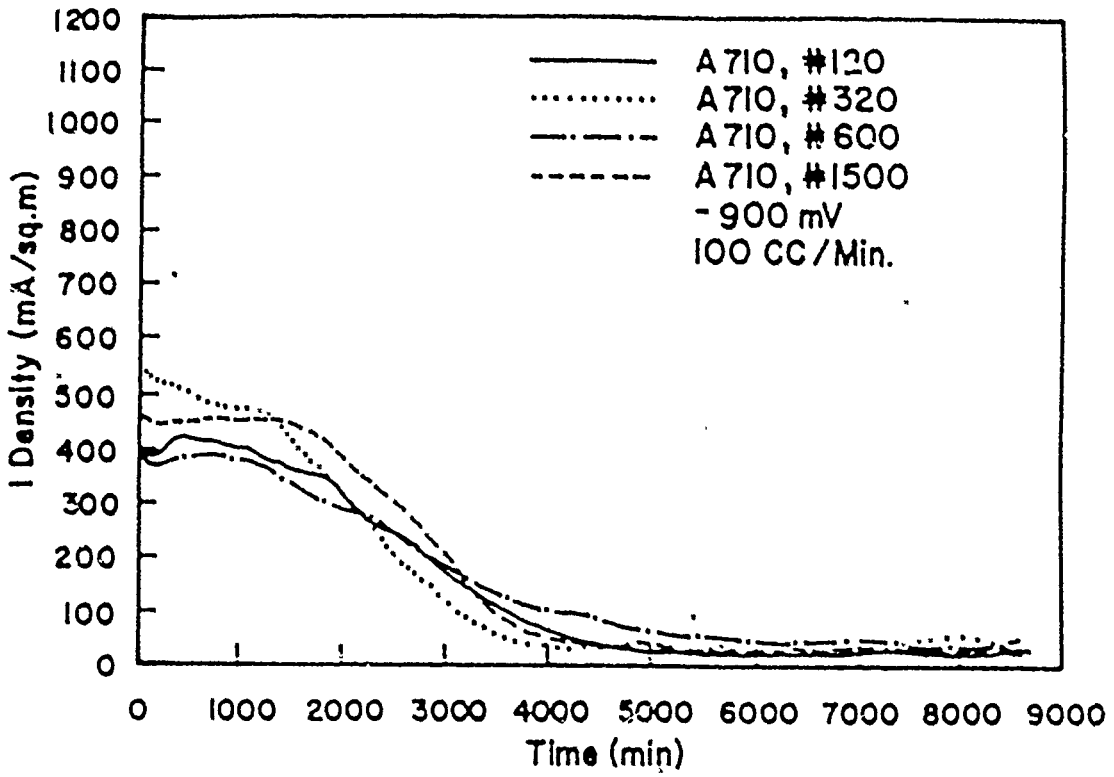

Figure 4. Current denisity versus time curves for A710 steel specimens of four different surface finishes concurrently polarized in seawater at -900 mV and 100 ml/min flow rate.

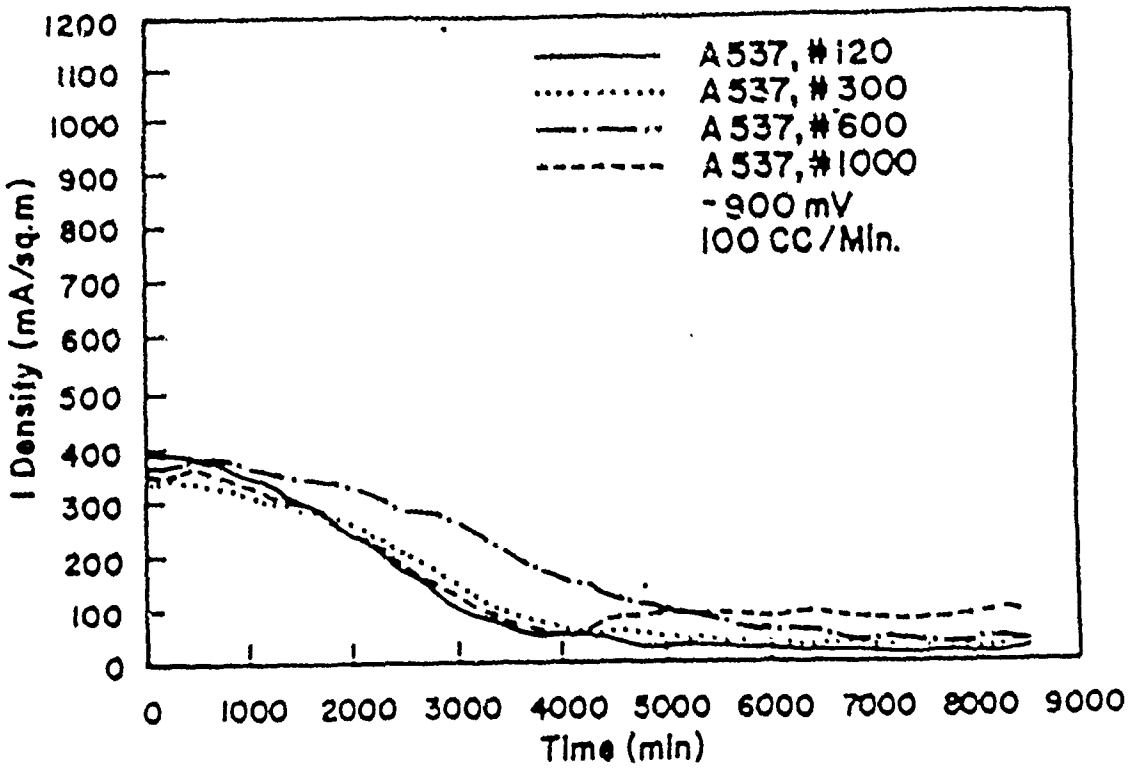

Figure 5. Current density versus time curves for A537 steel specimens of four different surface finishes concurrently polarized in seawater at -900 mV and 100 ml/min flow rate.

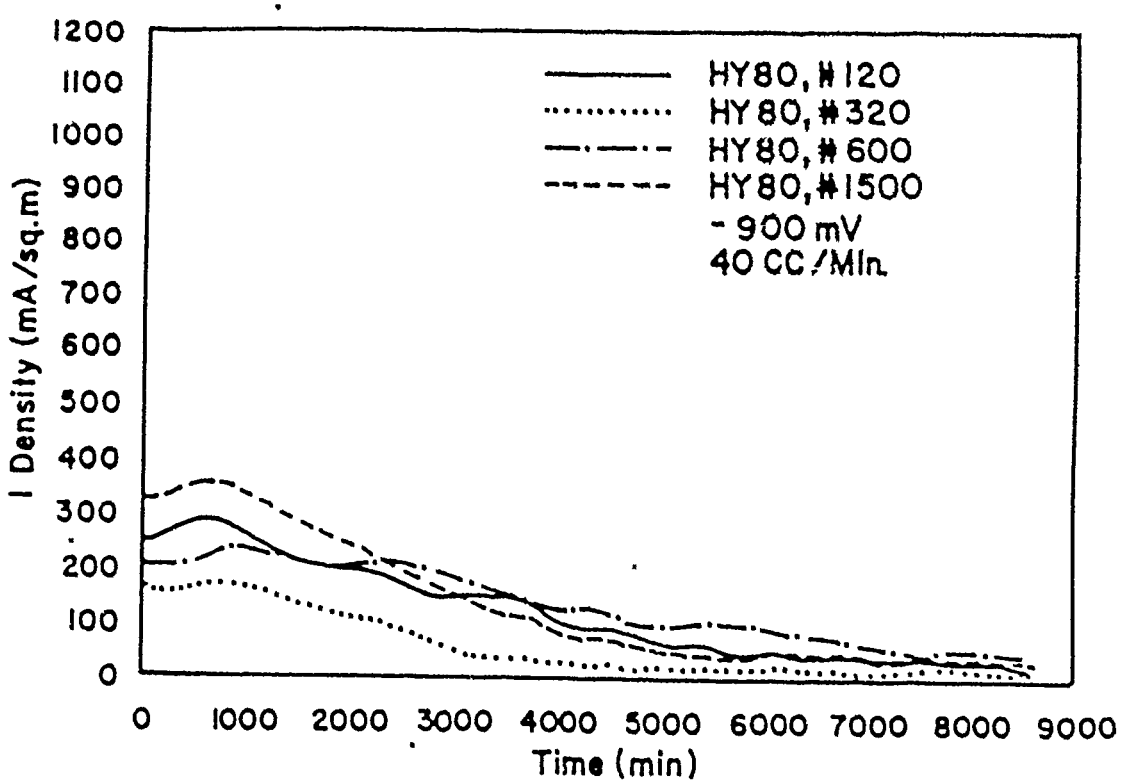

Figure 6. Current density versus time curves for HY80 steel specimens of four different surface finishes concurrently polarized in seawter at -900 mV and 40 ml/min flow rate.

Figure 7. Scanning electron micrograph of calcareous deposits on specimens polarized to -900 mV at seawater refreshment rate of 100 ml/min for 8400 min. (a) A710/#120 steel, (b) A537/#320 steel and (c) 1018/#120 steel.

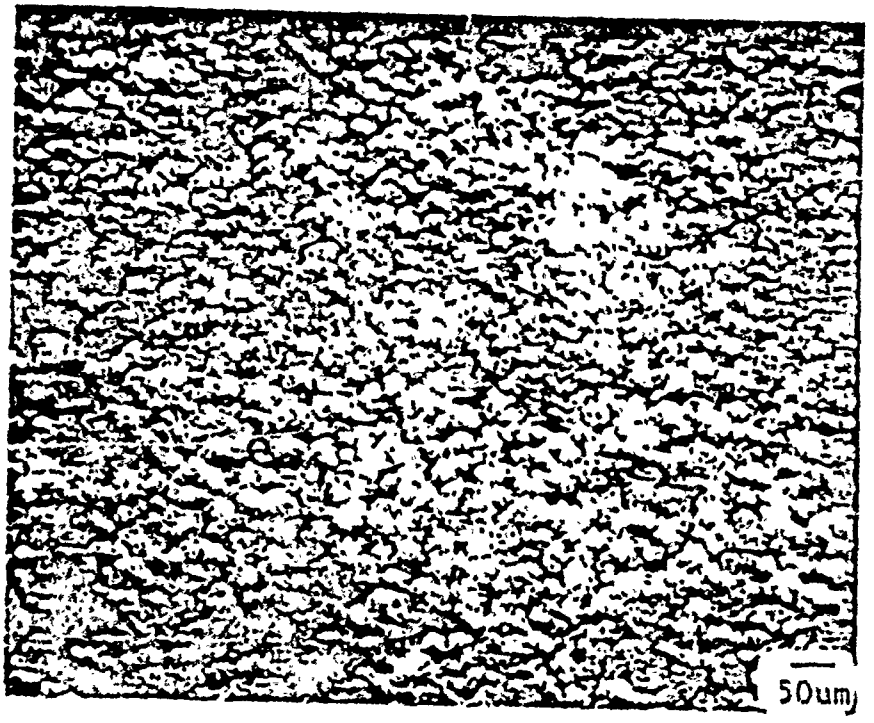

Figure 7 (b).

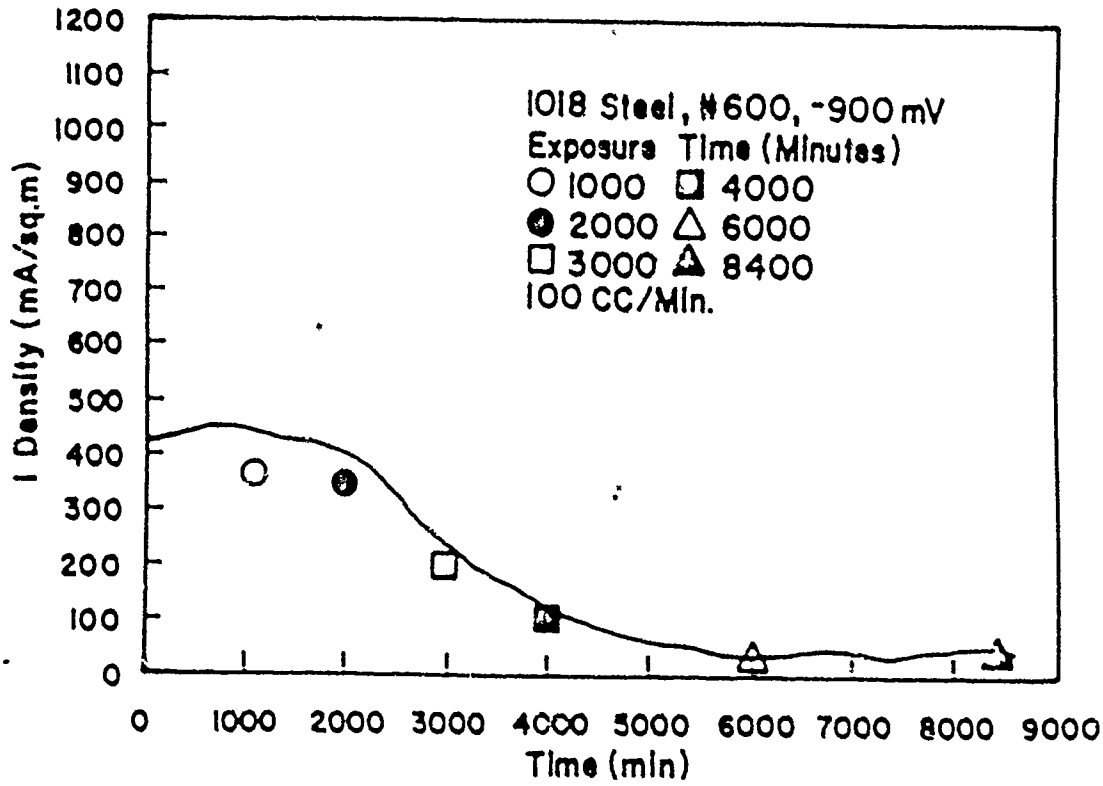

Figure 9. Current density versus time curve for 1018/#600 steel polarized to -900 mV for 8400 minues. Data points are the final i values for specimens exposed for 1000, 2000, 3000, 4000 and 6000 minutes.

Figure 10. Scanning electron micrograph of calcareous deposits on 1018/#600 steel polarized to -900 mV for 0.4 minutes at seawater refreshment rate of 100 ml/min.

Figure 11. Scanning electron micrograph of calcareous deposits on 1018/#600 steel polarized to -900 mV for two minutes at seawater refreshment rate of 100 ml/min.

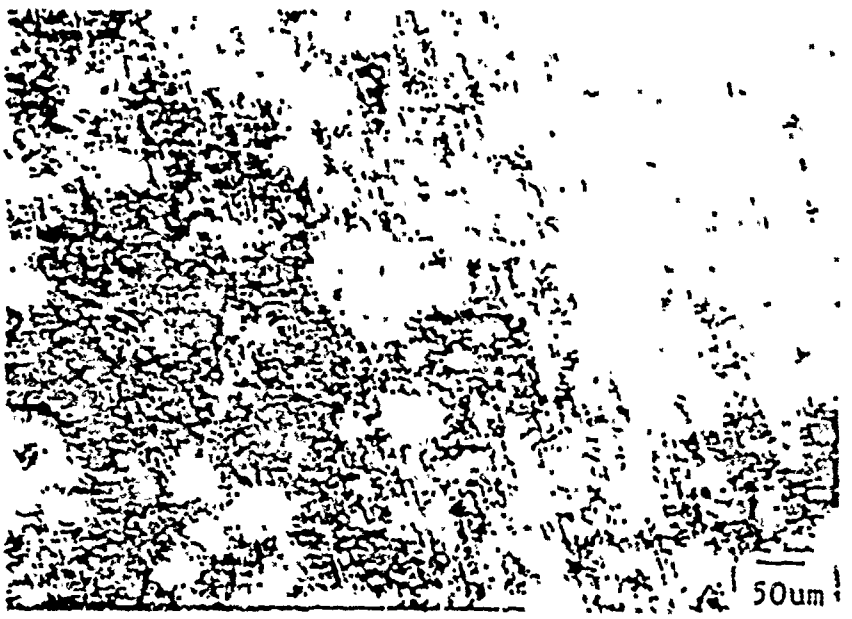

Figure 12. Scanning electron micrograph of calcareous deposits on 1018/#600 steel polarized to -900 mV for 60 minutes at seawater refreshment rate of 100 ml/min.

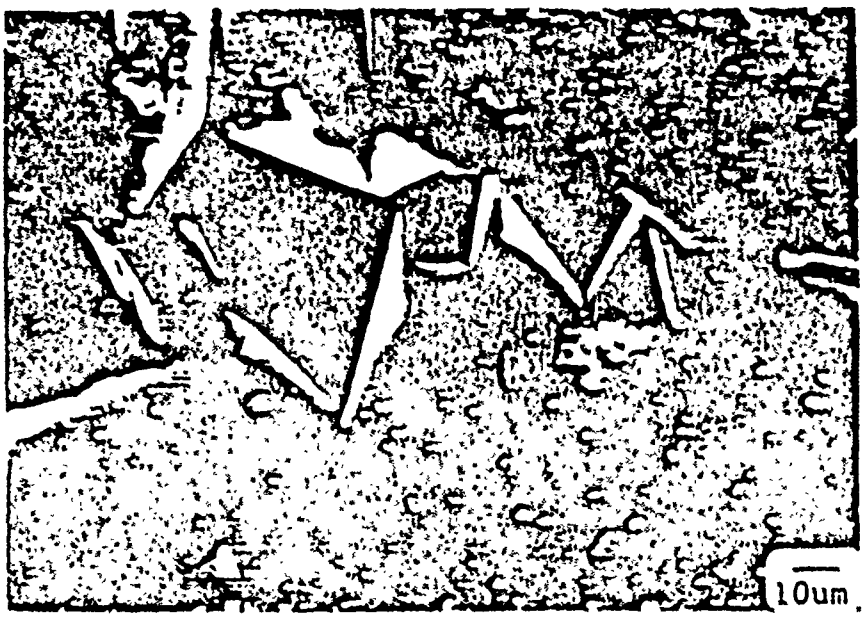

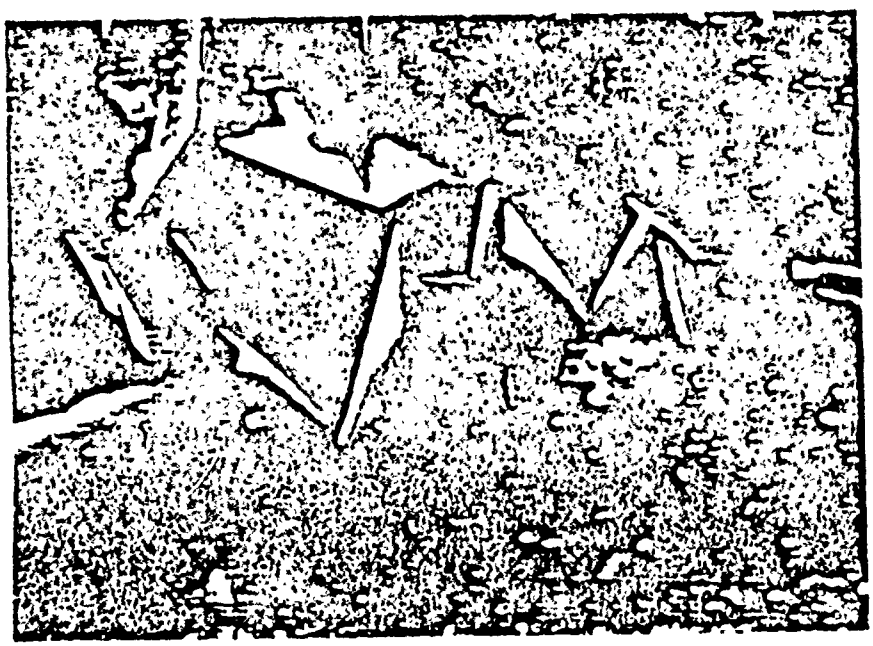

Figure 13. Scanning electron micrograph of partially disbonded calcareous film on 1018/#600 steel polarized to -900 mV for 15 minutes at seawater refreshment rate of 100 ml/min.

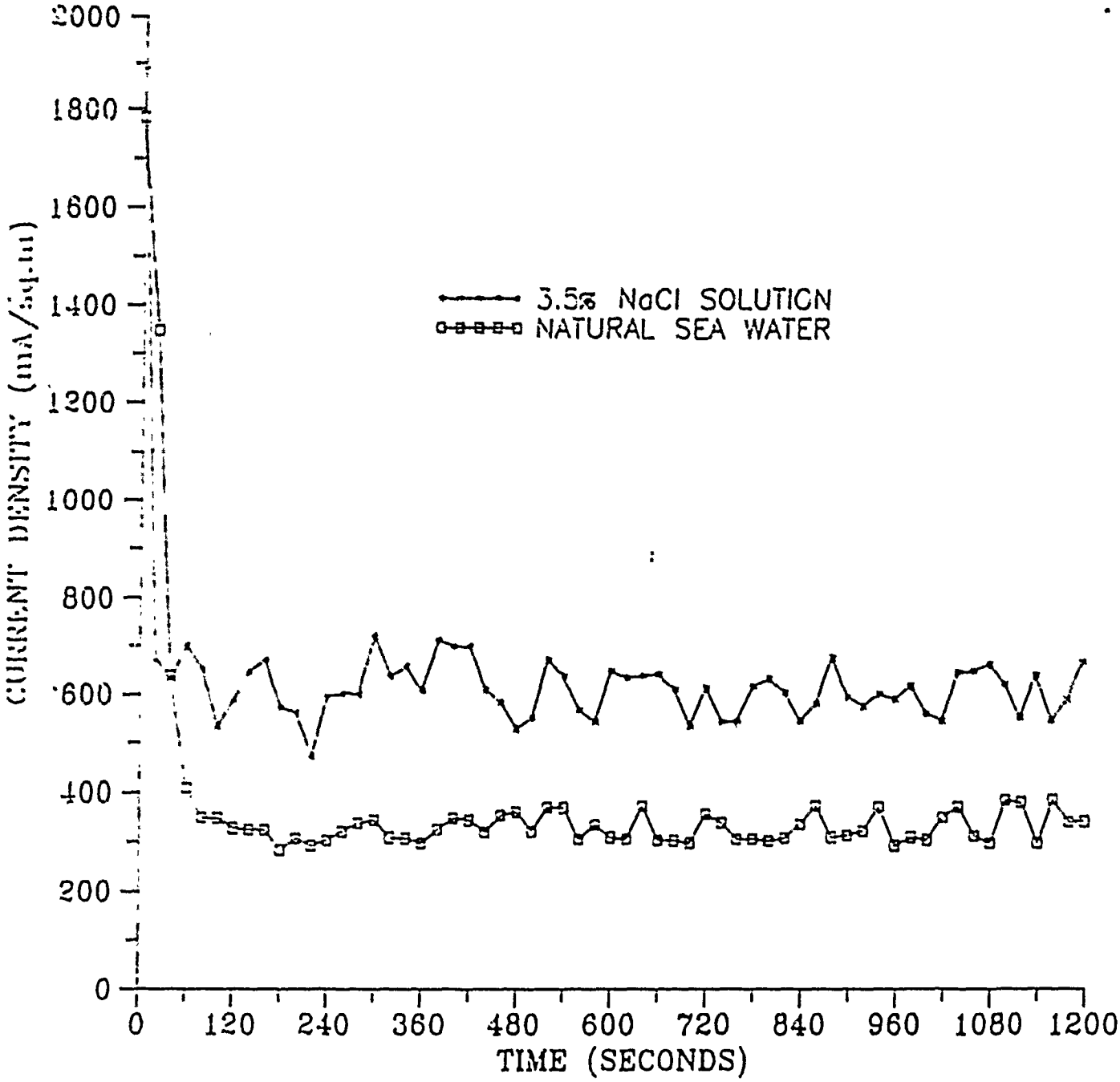

Figure 14. Current density versus time curves for polarization of HY80/#600 steel in 3.5 w/o NaCl and in natural seawater at -900 mV and refreshment rate of 100 ml/min.

(a)

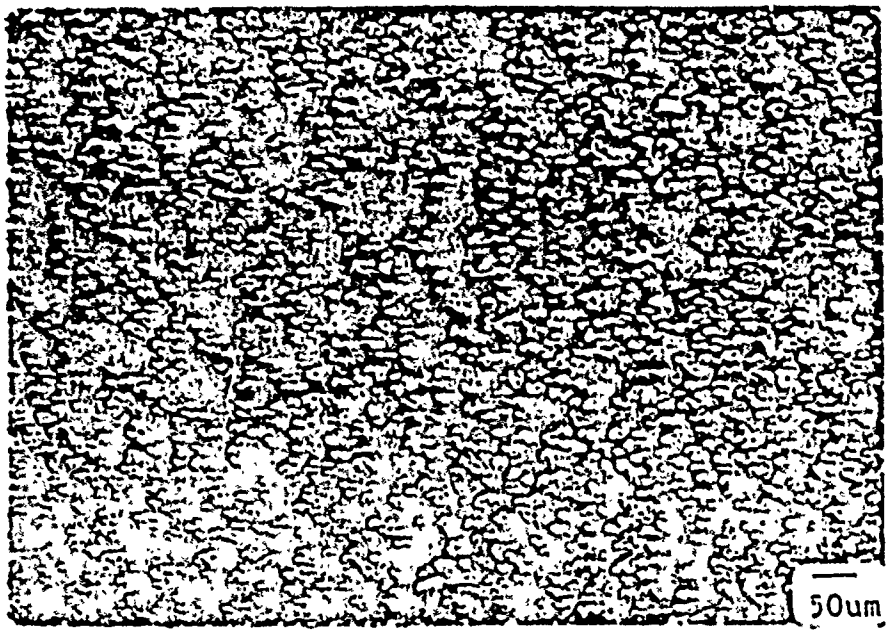

(b)

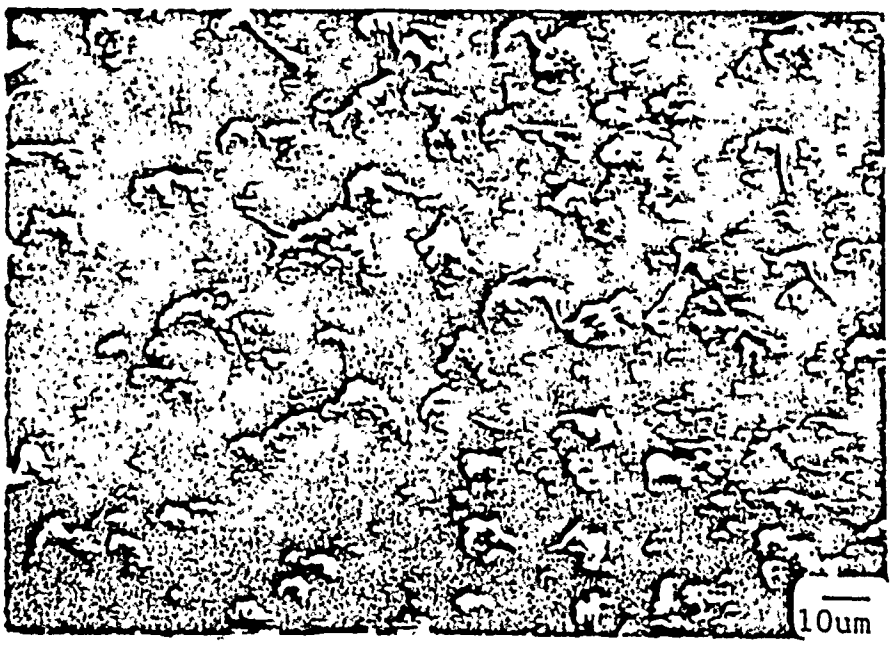

Figure 15. Scanning electron micrograph of Calcareous deposits on 1018/#600 polalrized to -900 mV for 1000 minutes at seawater refreshment rate of 100 m1/min. (a) low magnification and (b) high magnification.

(a)

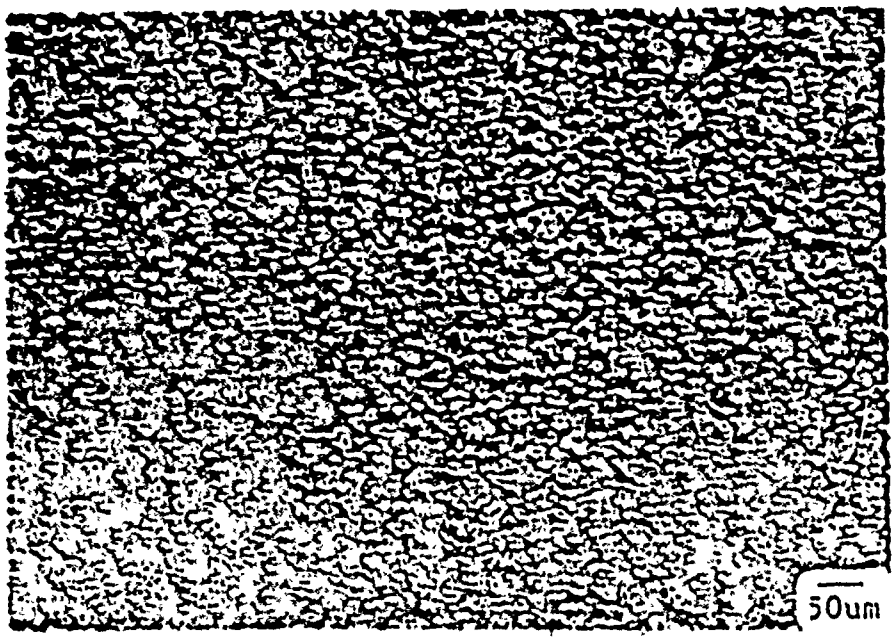

(b)

Figure 16. Scanning electron micrograph of calcareous deposits on 1018/#600 polarized to -900 mV for 2000 minutes at seawater refreshment rate of 100 ml/min. (a) low magnification and (b) high magnification.

(a)

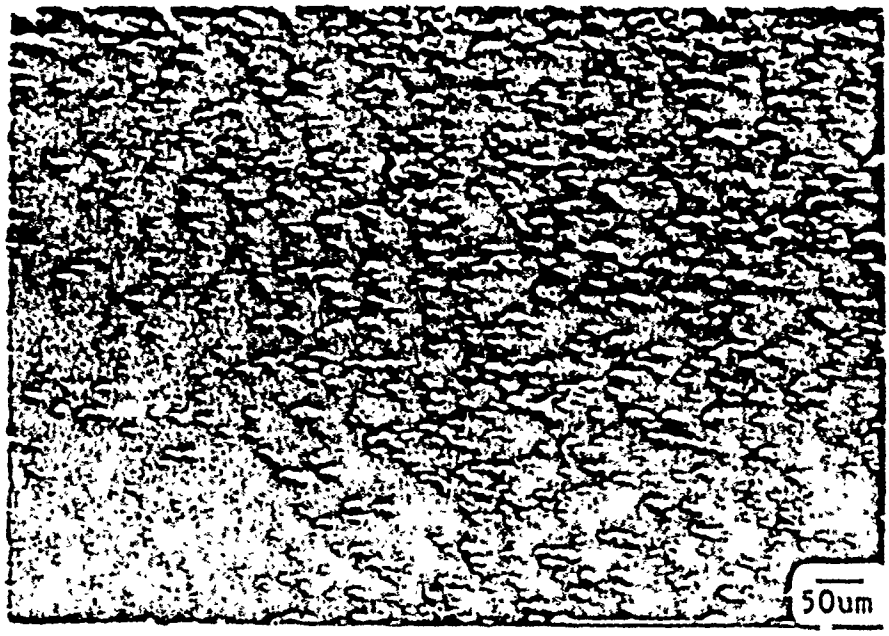

(b)

Figure 17. Scanning electron micrograph of calcareous deposits on 1018/#600 polarized to -900 mV for 3000 minutes at seawater refreshment rate of 100 ml/min. (a) low magnification and (b) high magnification.

(a)

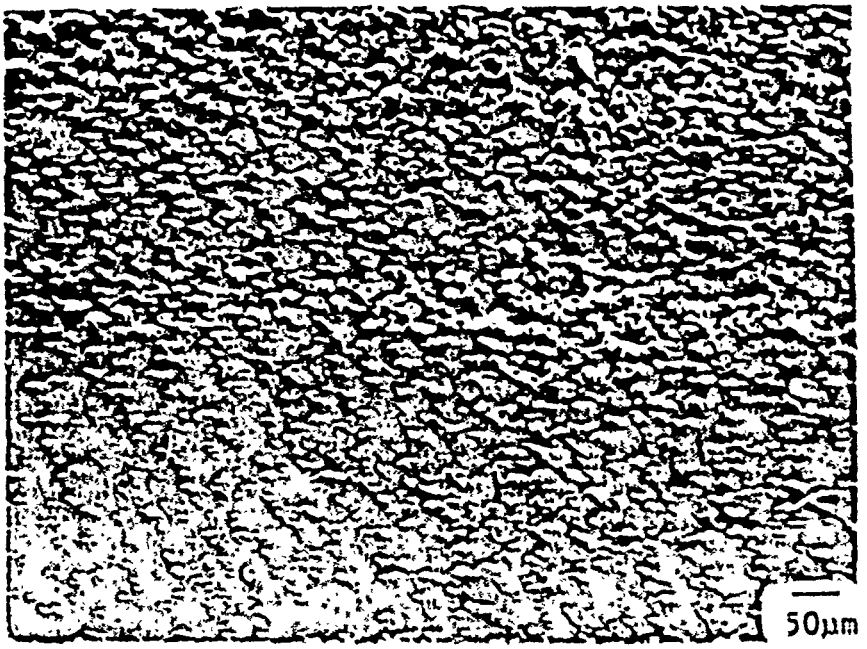

(b)

ure 18. Scanning electron micrograph of calcareous deposits on 1018/#600 polarized to -900 mV for 4000 minutes at seawater refreshment rate of 100 ml/min. (a) low magnification and (b) high magnification.

(a)

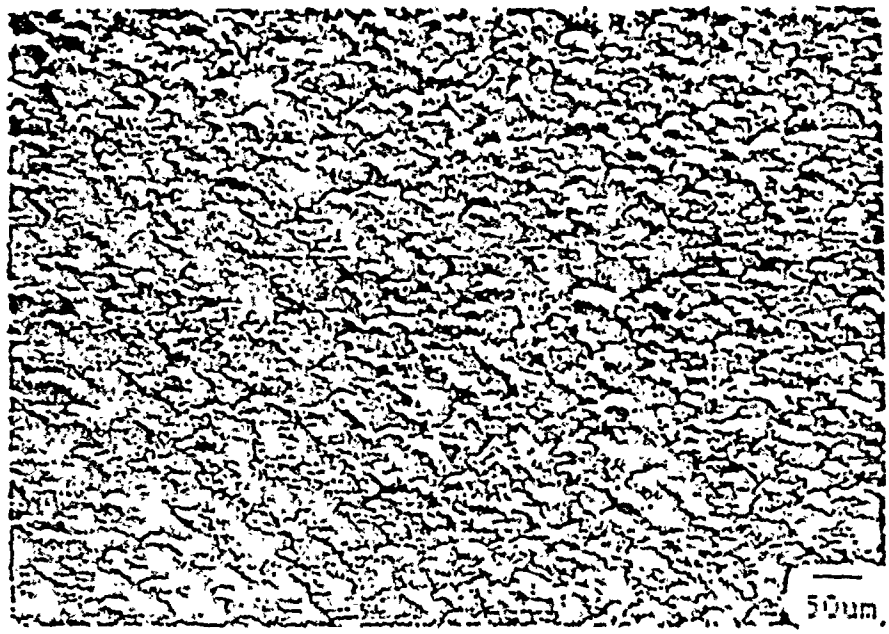

(b)

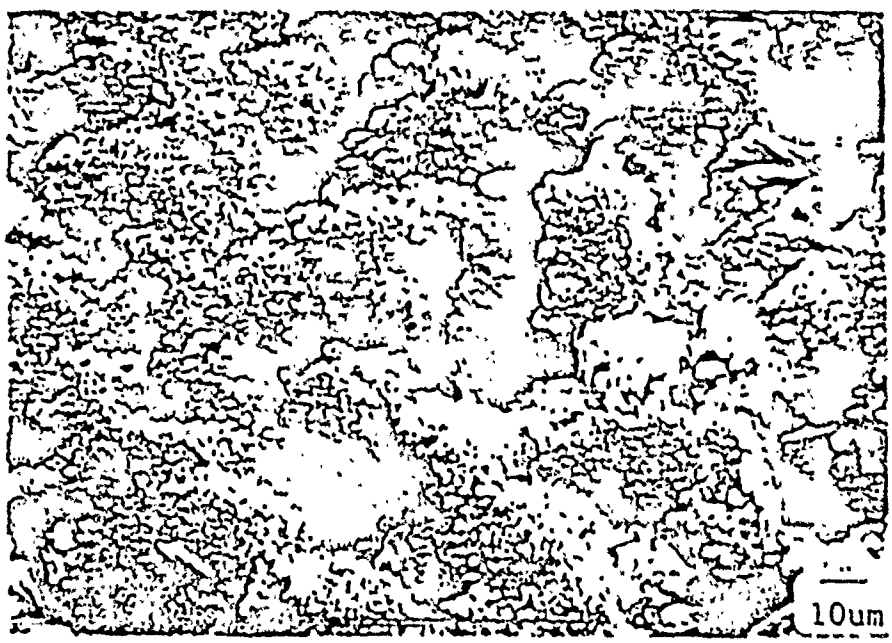

Figure 19. Scanning electron micrograph of calcareous deposits on 1018/#600 polarized to -900 mV for 6000 minutes at seawater regfreshment rate of 1000 ml/min. (a) low magnification and (b) high magnification.

(a)

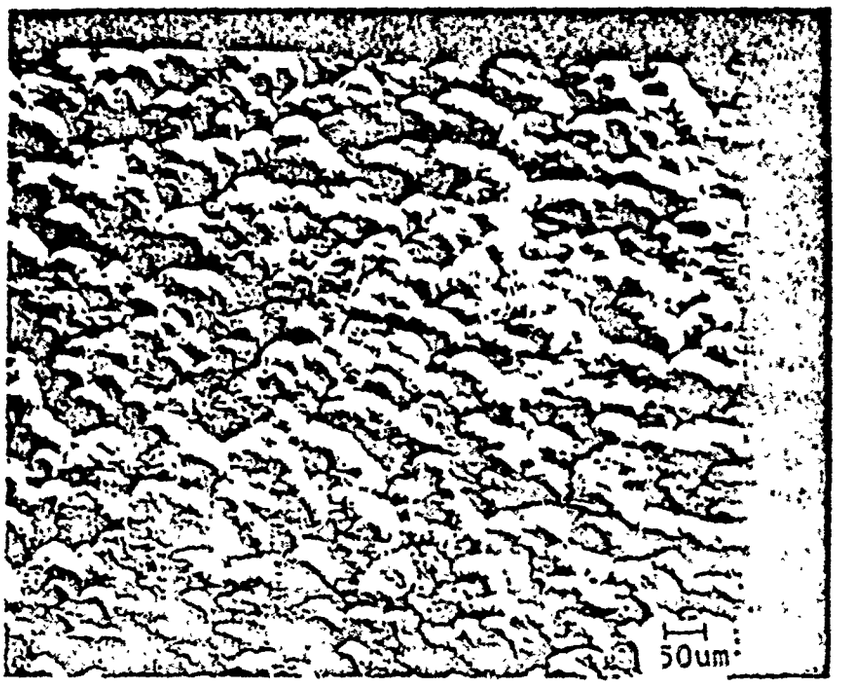

(b)

Figure 20. Scanning electron micrograph of calcareous deposits on 1018/#600 polarized to -900 mV for 8400 minutes at seawater refreshment rate of 100 ml/min. (a) low magnification and (b) high magnification.

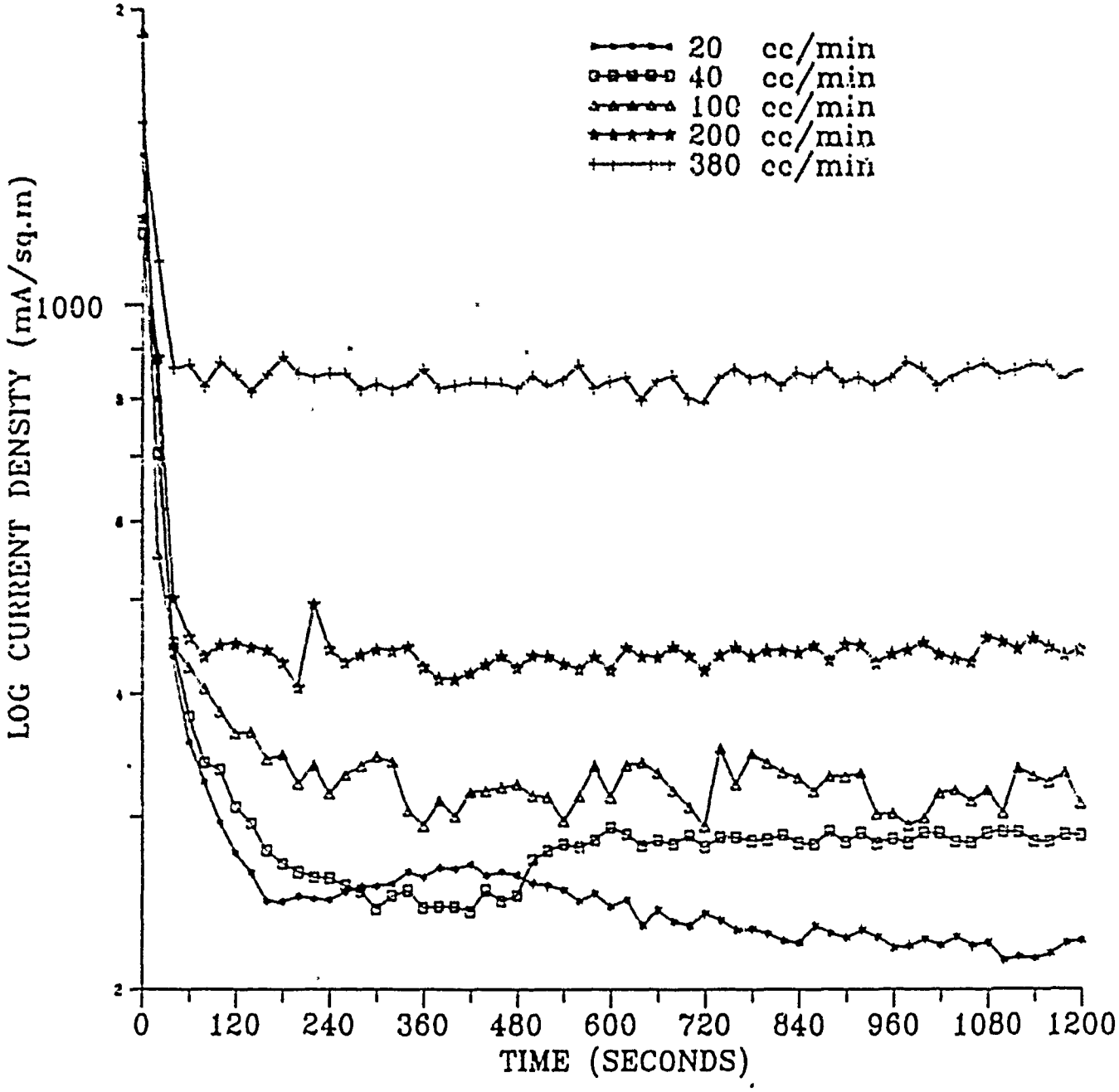

Figure 21. Current density versus time curves for HY80/#600 speciemns polarized to -900 mV at seawater refreshment rates of 20, 40, 100, 200 and 380 ml/min.

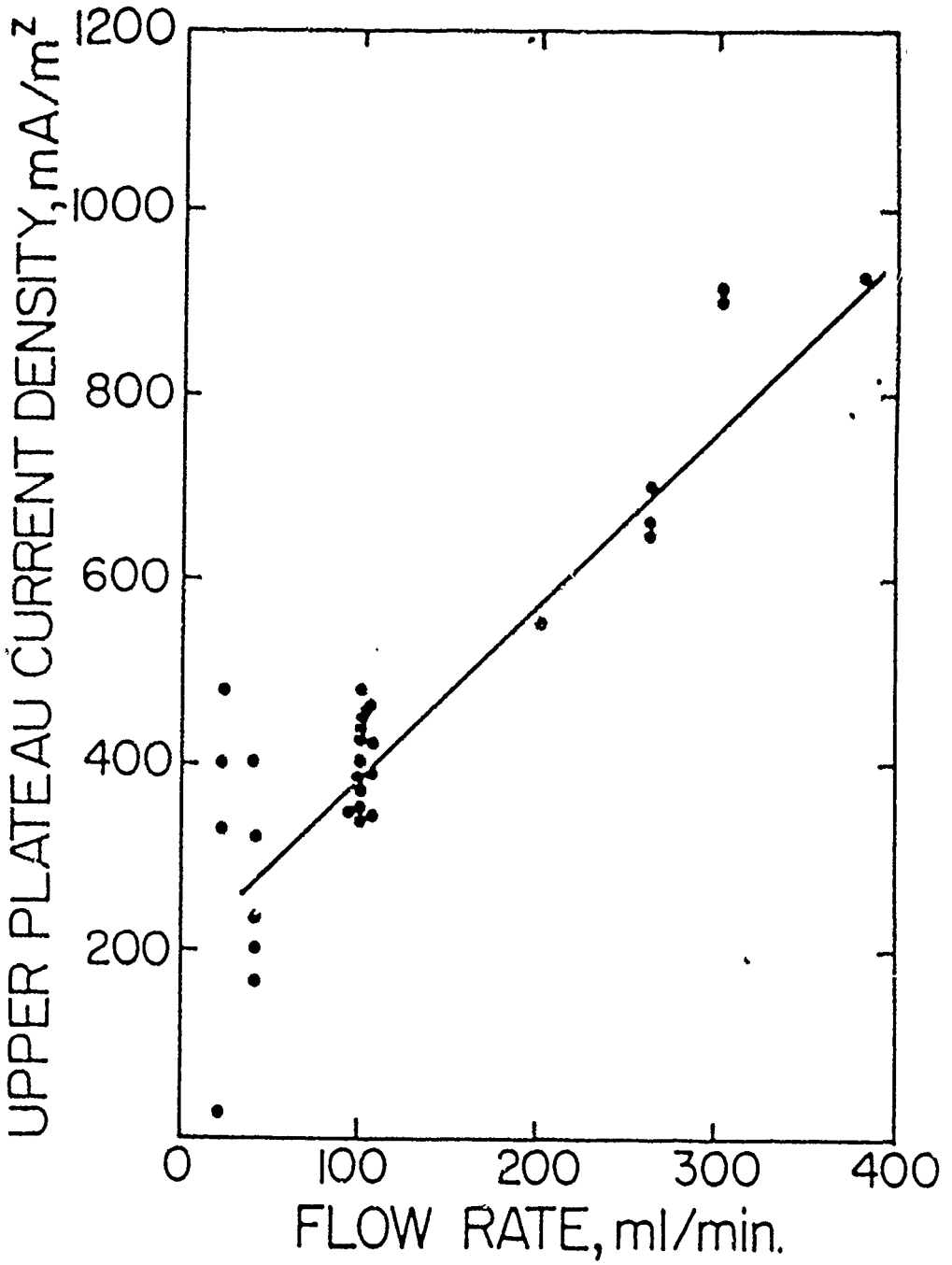

Figure 22. Plot of upper current density plateau values vs. seawater refreshment rate for all experiments.

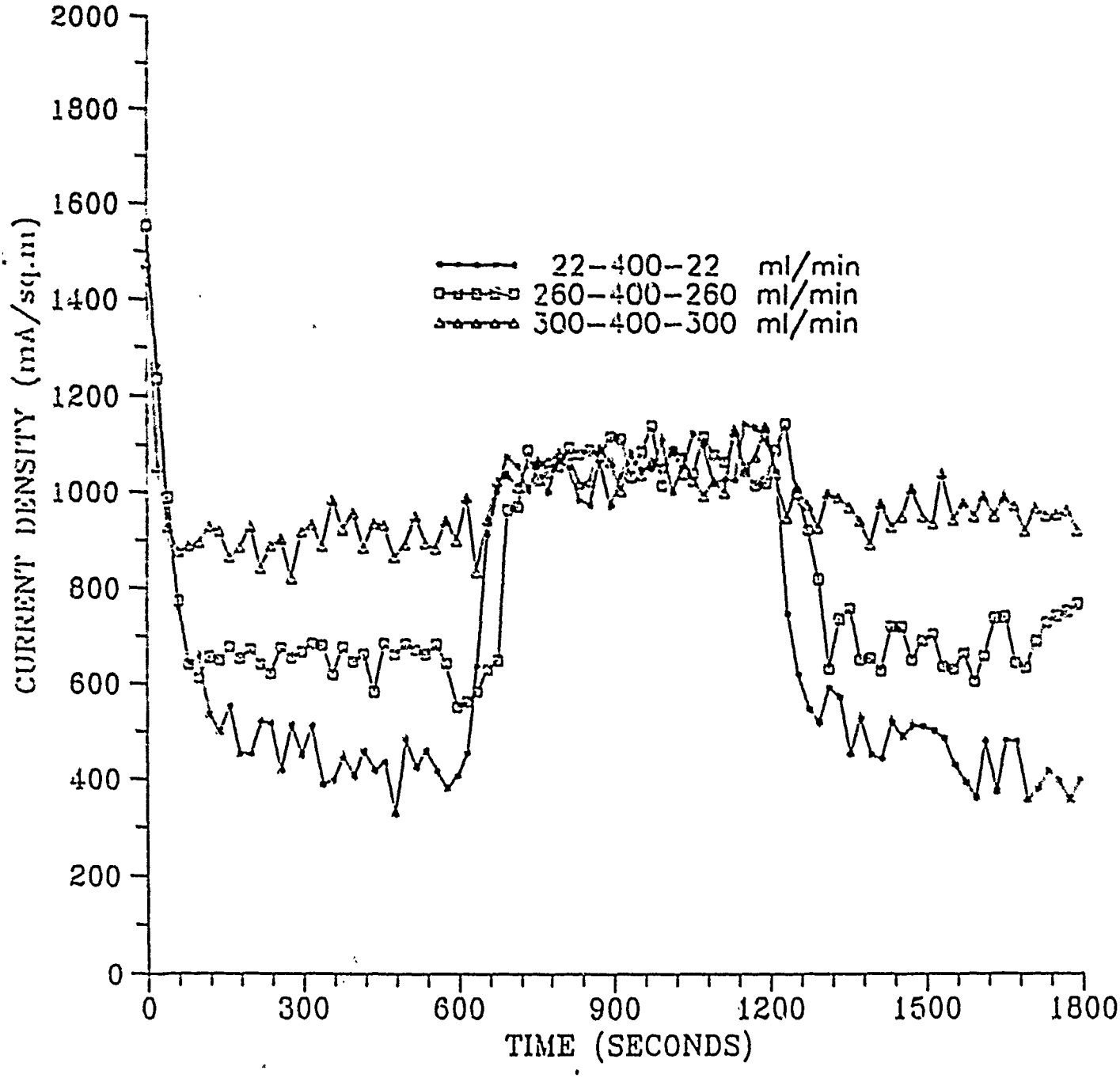

Figure 23. Current density versus time curves for HY80/#600 specimens polarized to -900 mV. Each specimen was exposed to flow rates of 22, 260, or 300 ml/min for the initial 10 min. followed by 10 min. at 400 ml/min and then returned to the initial flow rate.